International Journal of Multiphase Flow 47 (2012) 37–49

Contents lists available at SciVerse ScienceDirect

International Journal of Multiphase Flow

journal homepage: www.elsevier.com/locate/ijmulflow

Experimental statistics of droplet trajectory and air flow during aerodynamic fragmentation of liquid drops

A.K. Flock [a], D.R. Guildenbecher [a,b,*], J. Chen [b], P.E. Sojka [b], H.-J. Bauer [a]

[a] Institute of Thermal Turbomachinery, Karlsruhe Institute of Technology, Karlsruhe, Germany
[b] School of Mechanical Engineering, Purdue University, West Lafayette, USA

ARTICLE INFO

Article history:
Received 1 March 2012
Received in revised form 13 June 2012
Accepted 15 June 2012
Available online 23 June 2012

Keywords:
Aerodynamic fragmentation
Aerobreakup
Secondary atomization
Drop trajectory
Shadowgraphy
Particle image velocimetry

ABSTRACT

The deformation and fragmentation of single ethyl alcohol drops injected into a continuous air-jet is experimentally investigated. High speed shadowgraphy coupled with image contour recognition is used to record the instantaneous droplet shape, trajectory, velocity and acceleration, while particle image velocimetry captures the gas-phase flow-field around the drop. All experiments are repeated hundreds of times in order to determine the statistics based mean flow behavior. Two conditions are considered—one which leads to the bag breakup morphology and one leading to the sheet-thinning morphology. Comparing the two cases, no significant differences are observed in the structure of the gas-phase wake, indicating that gas-phase flow morphologies may not significantly affect the transition between liquid-phase breakup morphologies. The results of this investigation will be useful for the development and validation of simulation techniques.

1. Introduction

Liquid droplets are subjected to aerodynamic forces when the relative velocity between the drop and dispersed gas-phase is non-zero. These forces result in droplet deformation and, if sufficiently large, may lead to fragmentation. Such processes occur naturally during the falling of rain drops in the atmosphere (Villermaux and Bossa, 2009) and are applied in industry for the purpose of increasing liquid dispersal, enhancing evaporation, and reducing drop sizes (Nasar et al., 2002). A few typical applications include pharmaceutical sprays, diesel injectors, and air-assisted fuel atomizers in gas turbines. For spray applications the process is sometimes referred to as *secondary atomization*, which is distinct from the initial primary atomization of the liquid bulk (Lefebvre, 1989).

Fundamental experimental and theoretical investigations of aerodynamic drop deformation and fragmentation have been conducted by a number of investigators, and reviews are provided by Pilch and Erdman (1987), Hsiang and Faeth (1992), Gelfand (1996), Guildenbecher et al. (2009), and Theofanous (2011). Important non-dimensional parameters include the Weber number,

$$We = \rho_g u_0^2 d_0/\sigma, \tag{1}$$

defined as the ratio of initial disruptive aerodynamic forces to restorative surface tension forces, and the Ohnesorge number,

$$Oh = \mu_l/\sqrt{\rho_l \sigma d_0}, \tag{2}$$

which accounts for the effects of the liquid-phase viscosity. Here d_0 is the initial spherical drop diameter, u_0 is the initial relative velocity between the liquid- and gas-phase, σ is the surface tension, ρ is the density, and μ is the viscosity. The subscripts l and g specify liquid- and gas-phase properties, respectively. For impulsively loaded drops, of low to moderate viscosity ($Oh \lesssim 0.1$), extensive experimental evidence has shown that drops are unstable if We exceeds a critical Weber number, We_c. For the experimental configuration considered here, previous work indicates that $We_c \approx 9$ (Guildenbecher and Sojka, 2011). Note, other authors have reported slightly different values for We_c. These differences are most likely a function of the initial temporal history of droplet loading (Gelfand, 1996). Regardless, in all cases as We increases, multiple fragmentation morphologies have been identified, as shown in Fig. 1.

For practical applications, spray dynamics are often simulated using Eulerian–Lagrangian methods (Tanner, 1997; Trinh et al., 2007; Apte et al., 2009). These methods solve the gas-phase dynamics over a fixed grid and track the drop dynamics using Newton's second law coupled with models of aerodynamic drag, deformation, and fragmentation (O'Rourke and Amsden, 1987; Reitz, 1987; Ibrahim et al., 1993; Tanner, 1997; Schmehl, 2002; Apte et al., 2003). Often a large set of droplets or representative droplet parcels are simulated to obtain the statistics based mean flow behavior.

Experimental results are needed for the purposes of validation and model derivation. Furthermore, because the deformation and

* Corresponding author. Present address: Sandia National Laboratories, Albuquerque, NM, USA.
E-mail address: drguild@sandia.gov (D.R. Guildenbecher).

0301-9322/$ - see front matter © 2012 Elsevier Ltd. All rights reserved.
http://dx.doi.org/10.1016/j.ijmultiphaseflow.2012.06.008

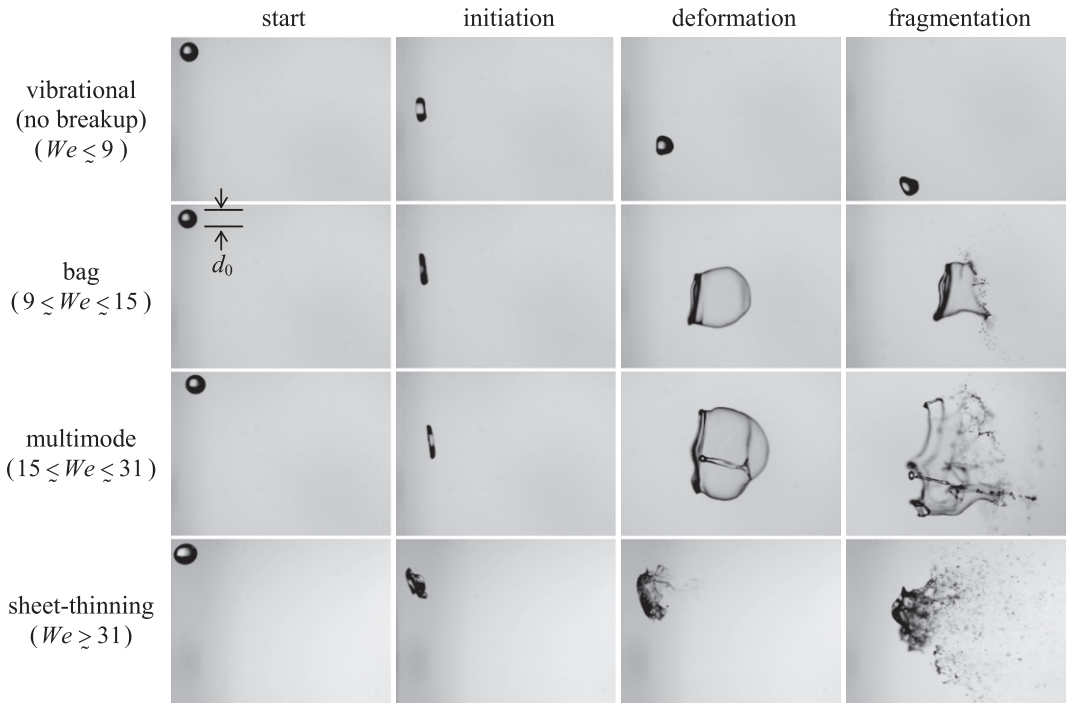

Fig. 1. Shadowgraphs of ethyl alcohol drops undergoing aerodynamic fragmentation. Time increases from left to right, disruptive forces increase from top to bottom. Images are from Guildenbecher and Sojka (2011) and were acquired using an experimental configuration similar to the present work.

fragmentation process is stochastic, experimental conditions must be repeated to ensure accurate representation of the statistical mean. Prior to this work, much of the available data have been obtained from experiments with individual drops impulsively loaded in a shock-tube (Hsiang and Faeth, 1992; Chou et al., 1997; Chou and Faeth, 1998; Dai and Faeth, 2001). While this method produces nearly ideal boundary conditions, the experiments are time-consuming, and repetition of conditions is necessarily limited. A few authors have attempted to increase experimental repetition by injecting a continuous stream of drops into a jet of air (Liu and Reitz, 1993; Hwang et al., 1996; Lee and Reitz, 2000; Park et al., 2006; Guildenbecher and Sojka, 2011), and their results confirm that the process is highly stochastic. Nevertheless, further experiments are needed which carefully account for the stochastic nature of the process. For this reason, the primary objective of the current work is to present experimental results for the mean behavior of droplets which are subjected to disruptive aerodynamic flow fields. Particular attention is paid to the initial stages of droplet motion and deformation.

In addition to recording the droplet trajectory and shape, this work quantifies the statistics of the surrounding gas-flow field. Such information is crucial for accurate definition of boundary conditions. Prior to this work, Inamura et al. (2009) conducted a related investigation using particle image velocimetry (PIV) to record the gas-flow around individual deformed drops. Only conditions leading to the first three morphologies shown in Fig. 1 were considered, and no attempt was made to quantify flow statistics. Therefore, the second objective of this work is to extend the results of Inamura et al. (2009) to include the sheet-thinning morphology and to quantify the mean flow field.

Finally, disagreement currently exists regarding the physical mechanisms responsible for the various breakup morphologies. For example, some have cited Rayleigh–Taylor instabilities to explain the morphological transition between the bag morphology in the second row of Fig. 1 and the multimode morphology in the third (Zhao et al., 2010, 2011; Theofanous, 2011), while Inamura et al. (2009) explained this transition based on observed differences in the gas-phase flow. Therefore, the third objective of this work is to provide additional experimental insight into the breakup morphologies.

The remainder of this work begins with a discussion of the experimental methods, including descriptions of the apparatus, flow conditions, high-speed shadowgraphy (HSS), and PIV configuration. This is followed with a section on the methods used to post-process the HSS and PIV results. Next statistical means and distributions are presented for experimental conditions leading to the bag and sheet-thinning fragmentation morphologies. Finally, the work concludes with a discussion of the results in the context of the stated objectives.

2. Experimental methods

Aerodynamically loaded droplets are created using the droplet generator and air-nozzle described by Guildenbecher (2009) and Guildenbecher and Sojka (2011). HSS is used to quantify the droplet morphology and trajectory, while the surrounding air flow field is measured using PIV. All measurements are automated to determine flow statistics.

2.1. Experimental configuration

The air-nozzle and droplet generator are shown schematically in Fig. 2a. The mass flow of air entering the nozzle is quantified by a Coriolis flow sensor (MicroMotion Inc. model F025S, estimated uncertainty ±0.01 kg/min). Before exiting the nozzle, air passes through a honeycomb and mesh to reduce turbulence. Fig. 2b and c shows typical mean and r.m.s. air velocities as measured with laser Doppler velocimetry (Dantec Dynamics FiberPDA) at x = 10 mm from the nozzle exit. Further details can be found in Guildenbecher (2009), where it is estimated that the boundary

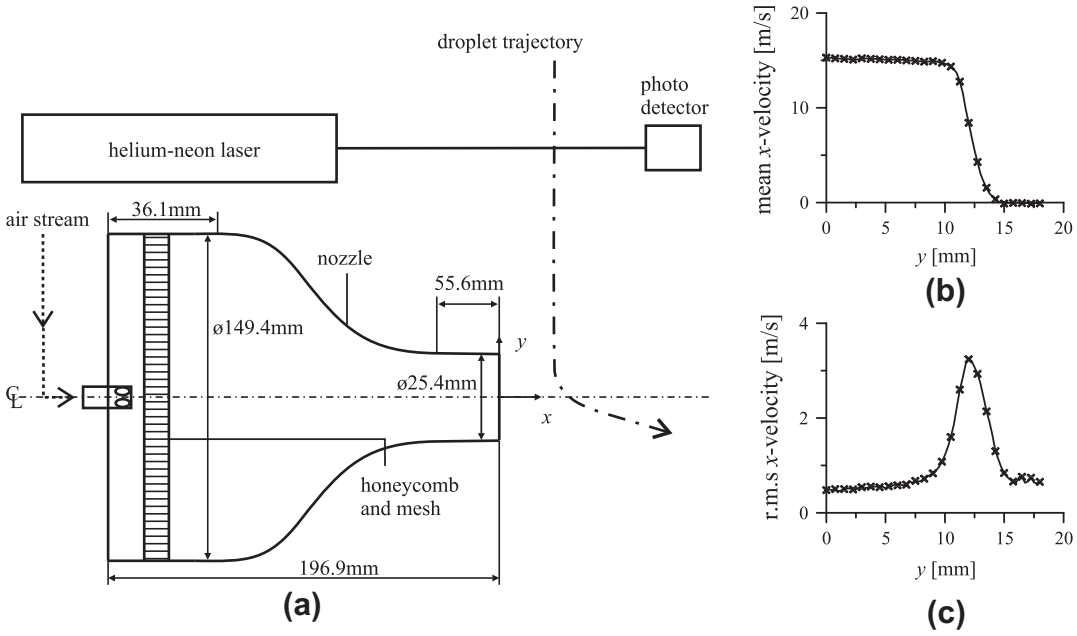

Fig. 2. (a) Configuration of the air nozzle and droplet generator, (b) mean and (c) r.m.s. air velocities in the x-direction measured at $x = 10$ mm and corresponding to an air mass flowrate of 0.50 kg/min (Guildenbecher, 2009).

layer thickness at the site of drop injection is approximately 3 mm for all conditions considered here.

Liquid droplets are produced from 200 proof, USP grade ethyl alcohol using a droplet generator operating in the periodic dripping regime (Clift et al., 1978). The generator is positioned to release droplets at approximately $y = 188$ mm above the centerline of the air nozzle. Initially the droplets fall through a nearly quiescent environment and are accelerated due to gravity. By neglecting the effects of aerodynamic drag during this period, the droplet's y-velocity upon entering the air-jet can be estimated by

$$v = \sqrt{2gh}, \tag{3}$$

where g is the acceleration due to gravity and h is the fall height (175 mm). Using Eq. (3), the estimated initial y-velocity is 1.85 m/s. Droplets are produced at a frequency on the order of 1 Hz, which is sufficient to ensure that the wake of the preceding droplet does not affect the behavior of the next droplet.

To capture the mean behavior of the droplets, the measurements are repeated several times. To do so, the data acquisition systems are triggered by the falling droplet. For this, the beam from a helium–neon laser (Uniphase Inc., model 1135P) is projected through the droplet trajectory onto a photo detector (Thorlabs Inc., model DET210). The intensity change, caused by the passing droplet, is highly repeatable and is used to trigger the oscilloscope, which sends a trigger signal to the timing unit of the PIV/HSS system.

2.2. Flow conditions

Two flow conditions are studied: one which results in the bag morphology and one which results in the sheet-thinning morphology. These conditions are summarized in Table 1. The mean and r.m.s air velocity in the x-direction along the nozzle centerline are taken from Guildenbecher (2009). For the calculation of non-dimensional parameters, the initial relative velocity, u_0, is assumed to be equal to the mean x-velocity along the centerline. The density, ρ_g, and viscosity, μ_g, of the gas-phase are 1.23 kg/m^3 and 18.27×10^{-6} N s/m^2, respectively, based on tables provided in Fox and McDonald (1998). The ethyl alcohol drops have a density, ρ_l, and viscosity, μ_l, of 789 kg/m^3 and 1.2×10^{-3} N s/m^2, respectively, based on properties provided in Riddick and Bunger (1970). The initial droplet diameter is around $d_0 = 2.3$ mm. Finally the surface tension, σ, is 2.23×10^{-2} N/m, again based on values provided by Riddick and Bunger (1970). In all cases, the temperature is assumed to be 298 K.

The Reynolds number shown in Table 1 quantifies the ratio of aerodynamic to viscous forces in the gas-phase,

$$Re_g = \rho_g u_0 d_0 / \mu_g. \tag{4}$$

Assuming the transient wake behavior of the deforming droplet is qualitatively similar to that of the steady flow past a sphere, at the values of Re_g given in Table 1, a turbulent wake is anticipated with the possibility of large scale vortical structures.

Finally, the effects of drop evaporation are estimated using the analysis given by Lefebvre (1989) for steady state evaporation in a convective flow field. Using standard thermodynamic properties and assuming the liquid- and gas-phases are isothermal, at the highest values of Re_g given in Table 1 the estimated droplet lifetime is on the order of 30 ms. This estimate does not account for the reduction in relative velocity due to aerodynamic drag, and the actual evaporation time is likely to be significantly longer. At this same condition, the experimental duration does

Table 1
Summary of experimental conditions.

Morphology	Air mass flowrate (kg/min)	Air velocity at $(x,y) = (10,0)$ mm		*We*	Re_g	*Oh*
		Mean (m/s)	r.m.s (m/s)			
Bag	0.35	10	0.15	13	1500	0.0059
Sheet-thinning	0.55	16	0.26	32	2500	0.0059

not exceed 6 ms (see Section 4), or 20% of the conservative droplet lifetime. Based on this, it is concluded that evaporation plays a relatively minor role in the phenomena considered here.

2.3. High-speed shadowgraphy (HSS)

Videos are acquired with a Vision Research Phantom v7 high-speed camera using the experimental configuration shown in Fig. 3. The camera is operated with a frame rate of 4000 fps, an exposure time of 30 μs, and a resolution of 800 × 600 pixels. The field of view is approximately 35 × 26 mm and is backlit by a collimated beam from a 1000 W arc lamp. The high-speed camera is triggered as described in Section 2.1 and records a video each time a trigger is received. The literature contains further information on the set-up and use of the high-speed camera (Guildenbecher, 2009; Flock, 2011).

2.4. Particle image velocimetry (PIV)

A PIV-system is added to the general experimental configuration as shown in Fig. 4. A double pulsed Nd:YAG laser (model New Wave Solo III) emits light at 532 nm which passes through a cylindrical lens to form a laser sheet with a thickness of about 1 mm. A mirror is used to direct the laser sheet into the test section. The air flow is seeded by an olive oil droplet generator (model 9307-6 from TSI Inc.), which is specified to generate tracer particles with a mean diameter of approximately 1 μm (verified with laser Doppler velocimetry). By controlling the ratio of "air with" to "air without" tracer particles entering the nozzle, the density of the seeding can be adjusted.

Images are recorded with a Flow Sense 2M 8 bit camera and consist of double frame pictures of 1600 × 1186 pixels. The field of view is approximately 14 × 10 mm. The PIV timing unit is also triggered using the method described in Section 2.1.

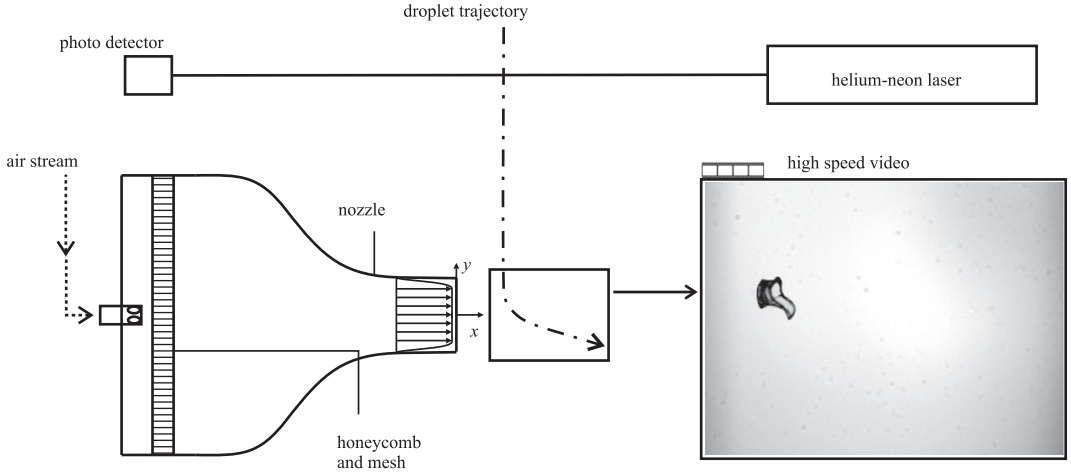

Fig. 3. Experimental configuration for high-speed shadowgraphy (HSS).

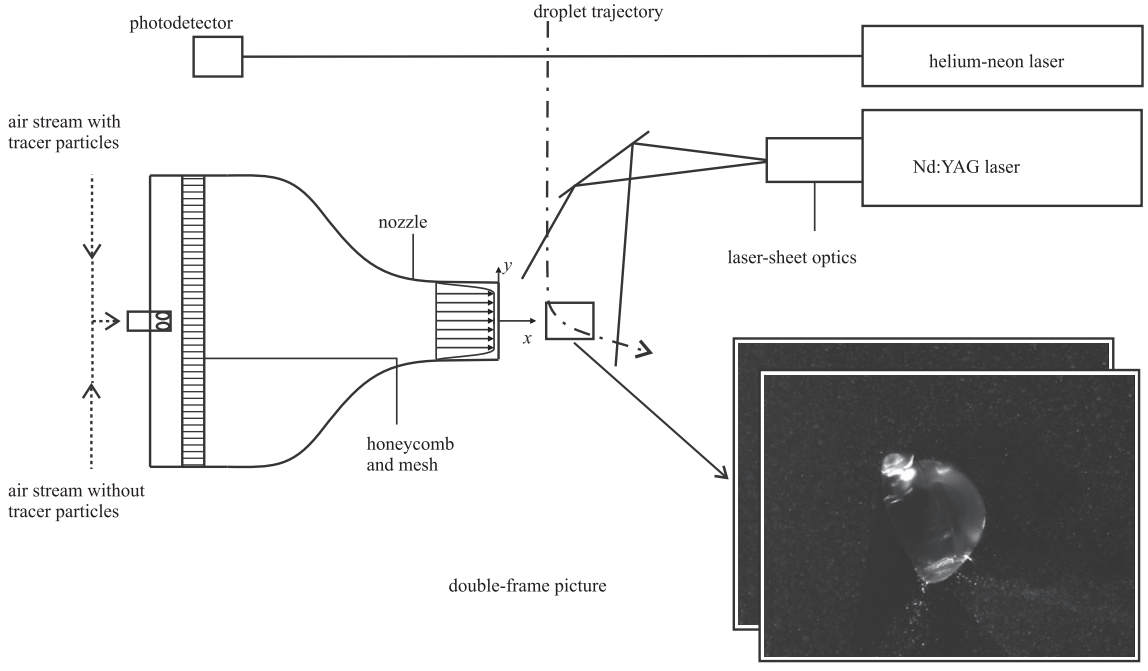

Fig. 4. Experimental configuration for particle image velocimetry (PIV).

Comparison of the raw PIV images, recorded with seeding particles, and the HSS images, recorded without seeding particles, reveals no significant differences in observed breakup morphologies. Consequently, the interaction of the oil seeding particles with the surface of the droplet is believed to have a minimal effect on the droplet deformation and breakup process. In addition, no PIV results are reported for times exceeding the droplet breakup time. As a result, errors which would result from velocity lag between the seeding particles and the relatively large secondary droplets (Driscoll et al., 2003) are not present in this work.

3. Data processing

The data are post-processed to calculate the mean droplet shape and trajectory as well as the average air-velocity field. Where applicable the 95% confidence interval for the true mean is calculated such that the true mean, μ_{true}, is found in a range of,

$$\mu_{true} \in \bar{a} \pm k_a S_a / \sqrt{N_a}, \tag{5}$$

where the standard deviation, S_a, is given by,

$$S_a = \sqrt{\sum_{i=1}^{N_a} \frac{(a_i - \bar{a})^2}{N_a - 1}}. \tag{6}$$

In these equations, a is the variable representing the measured quantity, a_i describes the measurement values at each realization, $\bar{a}$ the measured mean, and N_a is the number of realizations (American Society of Mechanical Engineers ASME, 2005). The variable k_a is dependent on the number of available realizations and decreases towards a value of 1.96 for infinite measurements. In the following sections, details are given on the calculation of mean droplet shape and trajectory followed by the post-processing of the PIV results.

3.1. High-speed shadowgraphy (HSS)

For each set of operating conditions, roughly 200 high-speed videos are acquired. Video frames are post-processed with a custom MATLAB® code (Müller et al., 2006) which detects the outer contour of the drop shadow as well as its geometric center. Ensemble averaging is then used to calculate the mean geometric center at each time-instant. This results in an average trajectory from which the mean velocity and acceleration are determined using a central-difference method. Also, the instantaneous droplet contour is used to define the droplet extent in the x- and y-directions, and ensemble averaging is used to find the mean extent at each time-instant.

Additionally, the following procedure is used to calculate a region which contains the entire droplet contour to within a specified probability. First, for every image frame, a matrix of the same size as the image frame (800×600 in this case) is initialized. Next, the area inside the measured droplet contour is assigned a value of one while the outside values are set to zero. Finally, for equal time instants, all matrices are added together and normalized by dividing by the number of videos. Thus one matrix for every time instant is calculated, and each entry describes the probability that the pixel lies within the shadowgraph contour. By detecting all entries above 5%, a region is determined such that all pixels within the region have a 5% or higher probability of lying within the shadowgraph contour. Hence a region is approximated where the droplets can be found with a 95% probability.

3.2. Particle image velocimetry (PIV)

To capture the temporal history of the air flow field around the deforming droplets, a delay is implemented between the triggering of the PIV system and acquisition of the double frame images. The process is illustrated in Fig. 5. For a given delay time, 2000 PIV realizations are recorded, and ensemble averaging is used to calculate the instantaneous mean flow field. By varying the delay time and repeating the acquisition, the mean flow field can be determined at any time instant along the trajectory. In the current study, six different delay times are investigated with a time gap between data sets of approximately 1–3 ms.

PIV image pairs are processed using the Dantec Dynamics FlowManager v4.71 software. An adaptive correlation with 25% overlap is performed. This PIV deconvolution technique begins with interrogation windows of 128×128 pixels, performs two refinement steps, and leads to a final vector field corresponding to interrogation areas

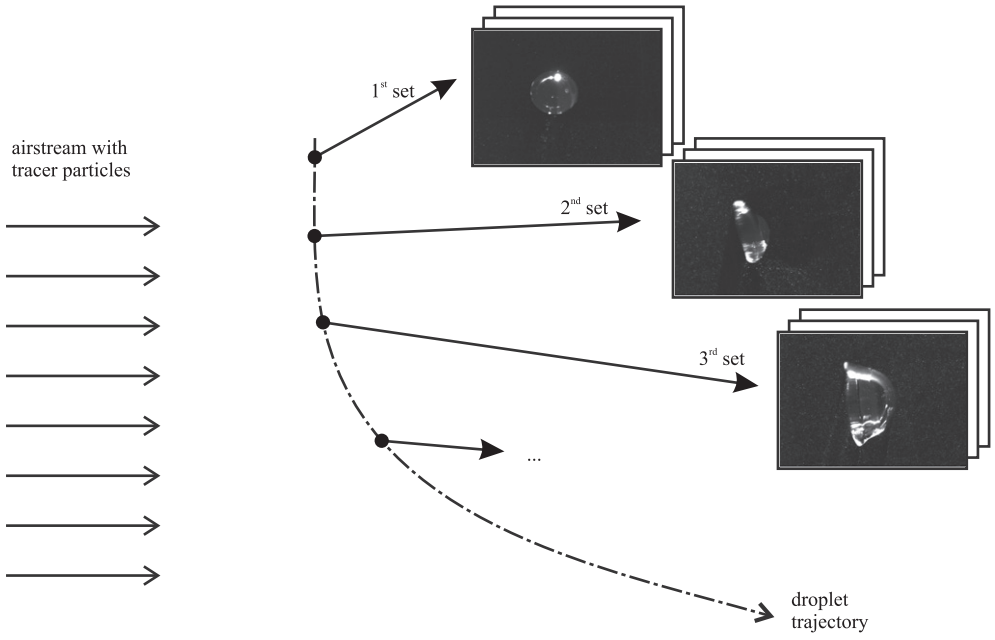

Fig. 5. PIV data acquisition method for calculation of ensemble averages.

of 32 × 32 pixels. A moving average filter is applied such that the maximum allowable velocity change within an area of 3 × 3 interrogation windows is 10%. In addition, no data is accepted when the peak in the correlation plane is less than 1.1 times the second highest peak. Inspection of the results reveals that these validation criteria filter out unrealistic data, while retaining valid velocity vectors.

To verify that 2000 realizations are sufficient to calculate converged statistics, an ensemble average was also calculated with the first 400 PIV realizations. Comparison of the ensemble average velocity fields for 2000 and 400 PIV realizations reveals little difference (Flock, 2011).

Finally, to match the field of view of the high speed videos to that of the PIV images, a calibration plate is affixed to the air nozzle, and images of this plate are acquired with both systems. In the results presented in the next section, instantaneous visualizations of the breakup morphology extracted from the high-speed videos are overlaid on the ensemble average velocity vectors acquired with the PIV technique. Invalid air velocity vectors within the droplet contours are removed.

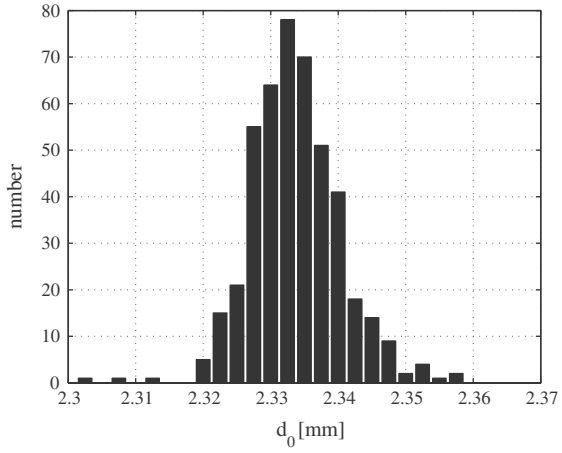

Fig. 6. Histogram of the initial spherical droplet diameters for all conditions considered.

4. Results

For each high-speed video, the droplet initial spherical diameter, d_0, is quantified using the MATLAB® code discussed in Section 3.1. Fig. 6 shows a histogram of d_0 from all of the recorded high-speed videos (the number of realizations, N_{d0}, is 453). The measured mean and standard deviation are $\bar{d}_0 = 2.3336$ mm and $S_{d0} = 0.0067$ mm respectively. Using Eq. (5) the associated 95% confidence interval of the true mean is $\bar{d}_0 = 2.3336 \pm 0.0006$ mm. Due to the narrow drop size distribution, higher-order mean diameters, which are sometimes reported in the literature (Lefebvre, 1989), are nearly identical to the reported number mean diameter.

4.1. Bag morphology

Using the configuration in Fig. 3, 208 high-speed videos of droplet fragmentation were recorded at the conditions given by the first row of Table 1. Fig. 7a shows the mean trajectory of the geometric center calculated using the methods outlined in Section 3.1, and Fig. 7b shows the corresponding standard deviations of position. In addition in Fig. 7a, the 95% confidence range is approximated by adding $\pm k_x \times S_{xi}$ and $\pm k_y \times S_{yi}$ to the average position in the x- and y-positions, respectively. In both figures, time $t = 0$ ms corresponds to an instant when the droplet just enters the air-flow field. Finally, due to difficulties calculating the shadowgraph contour, it is not possible to quantify the trajectory at times greater than those shown in Fig. 7.

As expected the standard deviation of droplet position is initially small, on the order of 0.1–0.2 mm or 4–9% of d_0. As the droplets propagate through the air-jet, the deviations grow due to random turbulent fluctuations and the stochastic nature of the fragmentation process. At the final times, the uncertainty of the x-position is roughly 2.5 times that of the y-position.

Note that the out-of-plane droplet position and associated uncertainties cannot be quantified with the current experimental configuration. However, because the mean gas-flow in the out-of-plane direction is approximately zero, similar to the flow in the y-direction, out-of-plane uncertainties can be estimated to be comparable in magnitude to those measured in the y-direction.

The mean x- and y-velocities, as well as the corresponding accelerations, are calculated by applying central differences to

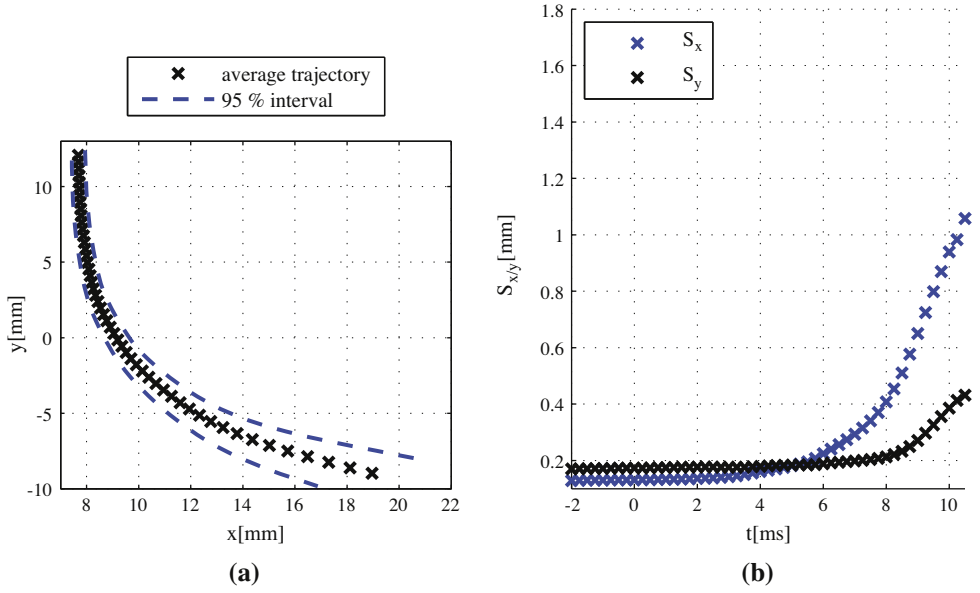

Fig. 7. (a) Mean trajectory and (b) standard deviation of droplet position in the x- and y-directions for the conditions leading to bag breakup.

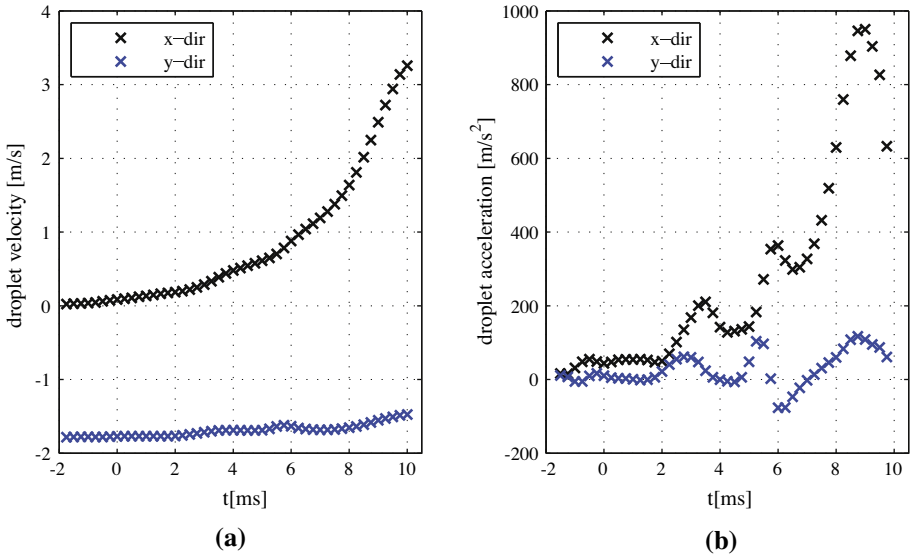

Fig. 8. Horizontal and vertical (a) velocities and (b) accelerations calculated with the central difference method for the conditions leading to bag breakup.

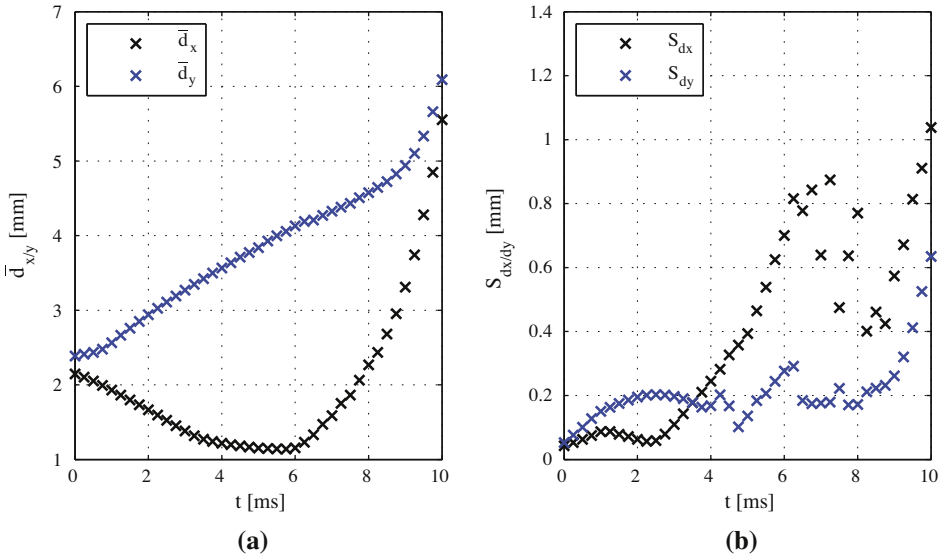

Fig. 9. (a) Mean droplet extent in the x-direction, $\bar{d}_x$, and y-direction, $\bar{d}_y$, and (b) the associated standard deviations for the conditions leading to bag breakup.

the position versus time data, and the results are plotted in Fig. 8. As expected, the initial mean droplet velocity in the y-direction corresponds closely to the estimated value given by Eq. (3), while the initial mean x-velocity is approximately zero.

After entering the air-jet, aerodynamic drag accelerates the droplets in the positive x-direction. In the y-direction, droplet acceleration tends to be slightly positive, against the direction of gravity. This may be attributed to droplet motion resulting in a component of the relative gas-phase velocity in the positive y-direction and thus a component of aerodynamic drag in the positive y-direction. Finally, it should be noted that after approximately $t = 5$ ms, a bag structure is formed and rapidly expands downstream (see Fig. 10). Although the bag has a large projected area, it has relatively little mass (Chou and Faeth, 1998). Consequently, the measured geometric center may no longer serve as a good approximation of the drop center of mass. Therefore, the reported acceleration may not correspond to physical acceleration of the drop center of mass for $t \lesssim 5$ ms. Further work is needed to quantify the differences between the reported geometric centers and the drop center of mass.

Fig. 9a shows the mean extent of the droplet contour in the x-direction, $\bar{d}_x$ and y-direction, $\bar{d}_y$, while Fig. 9b shows the associated standard deviations. The droplet initially contracts in the x-direction and expands in the y-direction. At $t = 6$ ms, contraction in the x-direction ceases and the bag begins to form (see Fig. 10) resulting in the observed increase in $\bar{d}_x$ after this time. In the literature, the time instant where the bag first begins to form is often used to define a so-called initiation time (Pilch and Erdman, 1987). Unfortunately, selection of this time directly from photographic results requires significant judgment, often resulting in somewhat arbitrary values with high uncertainty. As an alternative, Fig. 9a indicates that the time instant where $\bar{d}_x$ is minimized is a robust definition of initiation time.

Next, the air velocity field around the deforming droplet is quantified using the configuration in Fig. 4 and the methods outlined in Section 3.2. Fig. 10 shows a series of ensemble averaged

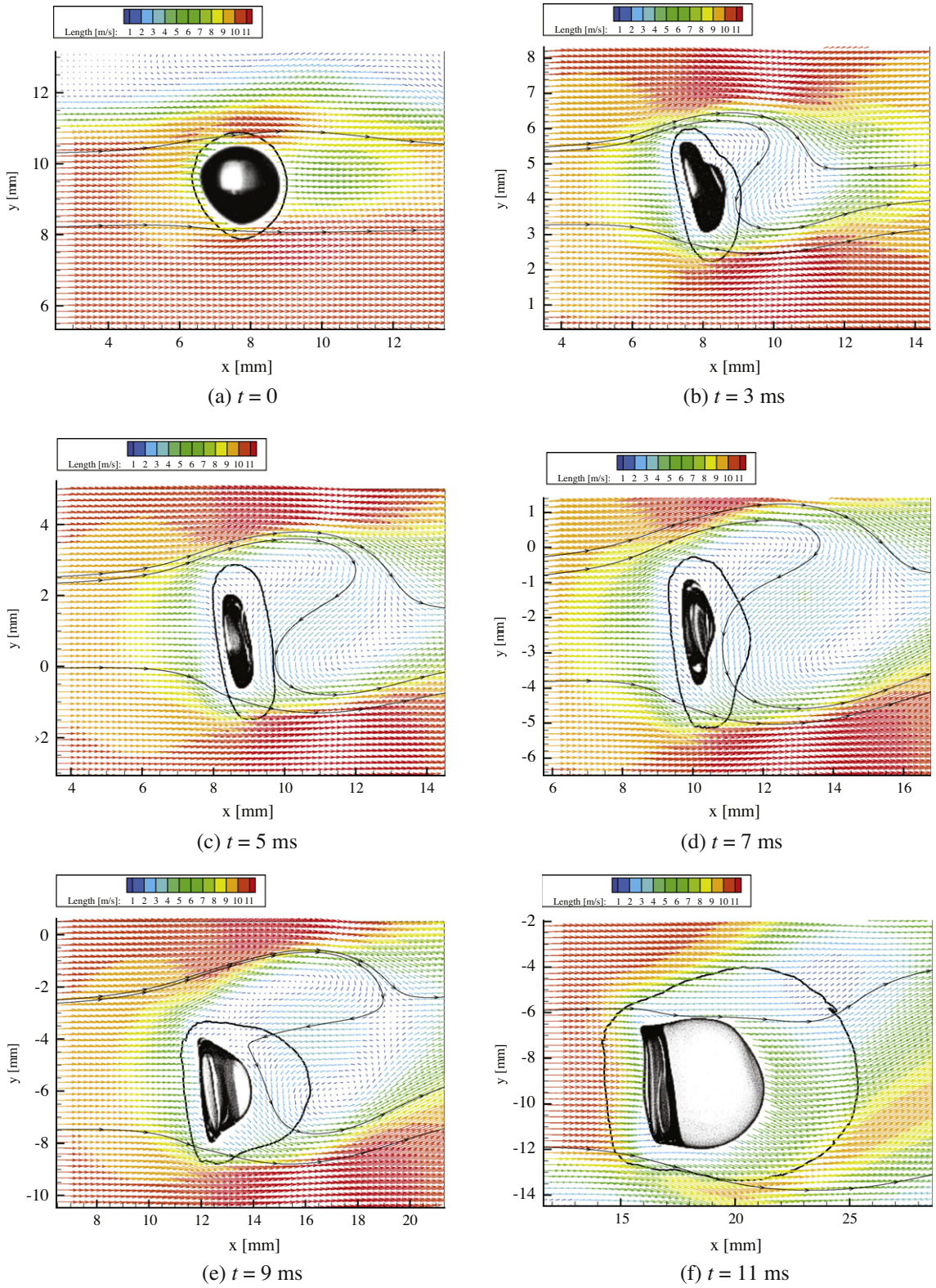

Fig. 10. Ensemble average velocity fields of 2000 PIV realizations at each instant of time for the conditions leading to bag breakup. Contour defines the region of 95% probability of the droplet outer-extent. A representative, instantaneous droplet shape is shown at the approximate mean droplet location. Note the shift in horizontal and vertical axes between figures. (For interpretation to colours in this figure, the reader is referred to the web version of this paper.)

results of 2000 realizations at each time point. Time $t = 0$ ms corresponds to the same initial time point given in previous figures. Select streamlines are shown to highlight the mean flow behavior. In addition, a contour is shown which represents the region where the droplet outer-extent can be found to within 95% probability as calculated using the methods outlined in Section 3.1. Finally, a representative, instantaneous droplet image taken from a high-speed video is shown at the approximate mean droplet location. PIV results within the drop are assumed invalid and are not shown.

The first image of the sequence (Fig. 10a) is acquired at an instant shortly after the droplet has entered the airstream. The freestream velocity of approximately 10 m/s is visible for $y < 7$ mm; a decrease in x-velocity, due to the mixing layer of the air-jet, can be seen in the region defined by 10 mm $< y <$ 12 mm. With increasing time the droplet deforms and is transported downstream. A wake is detected at approximately 3 ms after the first image (Fig. 10b). At 5 ms after the first image (Fig. 10c), a distinct region of backflow is observed within the wake region. The backflow velocity is approximately 3–4 m/s, which corresponds to 30–40% of the free-stream velocity. This region of backflow persists as the bag begins to develop (Fig. 10d and e). Finally, with a further growth of the bag 11 ms after the initial image the recirculation zone is no longer detected (Fig. 10f). The relatively low air velocities in the lower left corner of Fig. 10f arise from the mixing layer of the air-jet. At later times, the droplet may leave the air-jet; nevertheless, the high-speed videos confirm that the droplets eventually fragment at these operating conditions.

It should be noted that a number of factors contribute to the overall uncertainty of the PIV results given in Fig. 10. Typical PIV noise sources—such as background noise, peak locking effects and displacement gradients (Raffel et al., 2007)—are reduced but not eliminated by the use of advanced commercial cross-correlation algorithms. Additional noise sources arise from the unique nature of this multiphase flow measurement. First, as seen in the sample PIV images shown in Figs. 4 and 5, the liquid drop reflects and refracts the laser sheet, resulting in bright spots and some local CCD blooming. This tends to obscure valid data near the drop. Second, a shadow is formed in the region of the laser sheet behind the drop. Pre-processing is used to reduce variations in background intensity; nevertheless, this shadow can be expected to increase noise in this area. Lastly, variation of the drop position between realizations (see Fig. 7b) and subsequent averaging may tend to reduce persistent flow structures—such as wake vortices—if they exist. Further work is needed to quantify these sources of uncertainty.

To illustrate differences between the instantaneous PIV realizations and the averaged results, Fig. 11 shows two instantaneous

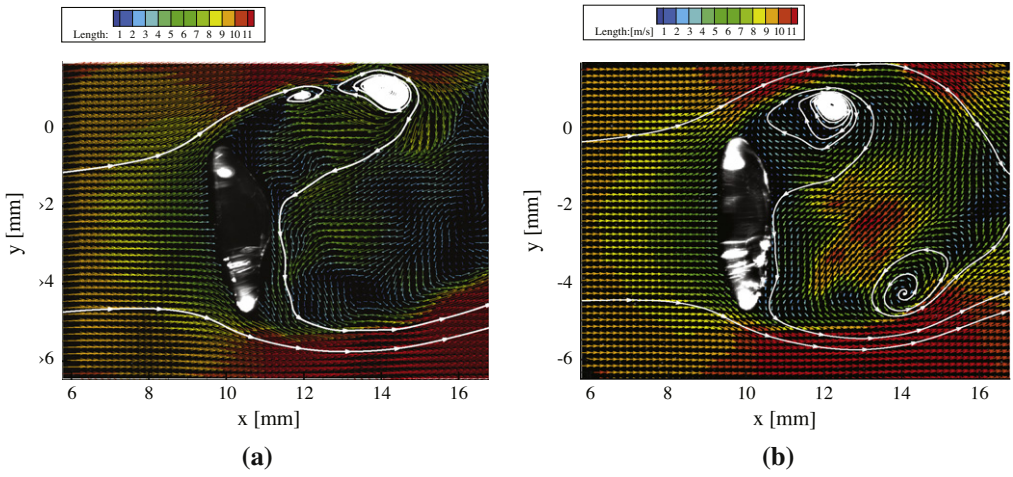

Fig. 11. Instantaneous PIV realizations at $t = 7$ ms for the conditions leading to bag breakup. (For interpretation to colours in this figure, the reader is referred to the web version of this paper.)

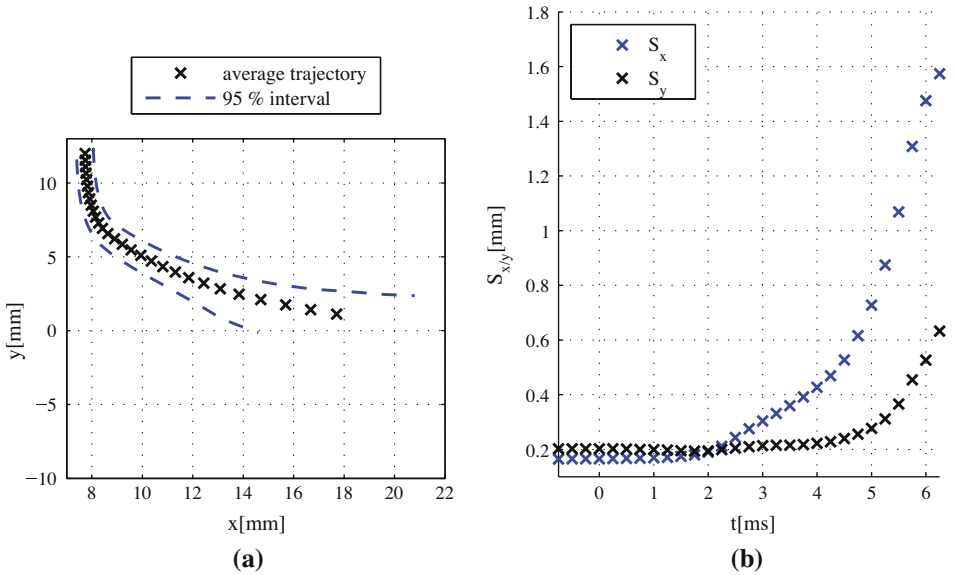

Fig. 12. (a) Mean trajectory and (b) standard deviation of droplet position in the x- and y-directions for the conditions leading to the sheet-thinning morphology.

PIV realizations at $t = 7$ ms. Compared to the mean flow (Fig. 10d), the instantaneous realizations display distinct turbulent eddies, as highlighted by the selected streamlines.

4.2. Sheet-thinning morphology

In this subsection, results for the experimental conditions leading to the sheet-thinning morphology are presented. The presentation closely follows that of the bag breakup morphology given in the previous subsection.

Fig. 12 shows the mean trajectory and standard deviations of position calculated from 245 high-speed videos of droplet fragmentation at the conditions given by the second row of Table 1. Similar to the bag breakup case, the standard deviations of droplet position are initially on the order of 0.1–0.2 mm and increase as the droplet propagates through the air-jet. At the final times, the uncertainty of the x-position is roughly 2.5 times that of the y-position, also similar to the bag breakup case.

Fig. 13 shows the mean x- and y-velocities calculated by applying central differences to the position versus time data. Once again, the initial droplet velocity is in close agreement with the estimate given by Eq. (3). Due to the higher gas-phase velocities, droplet acceleration in the x-direction is greater in magnitude as compared to the bag morphology, while the temporal history of the y-velocity closely resembles that of the bag breakup case. Again, positive y-acceleration is observed. Finally, it should be noted that the measured acceleration after $t = 3$ ms may not correspond to the physical acceleration of the drop center of mass for the same reasons given above in the bag breakup case.

Next, Fig. 14 shows the mean and standard deviation of the droplet extents with respect to time. Again, minimization of $\bar{d}_x$ can be used to define the initiation time at approximately 3 ms.

Fig. 15 shows a series of ensemble averaged air flow-fields corresponding to the sheet-thinning morphology. Time $t = 0$ ms corresponds to the same initial time point given in previous figures. At the first time instant (Fig. 15a), the freestream velocity of about

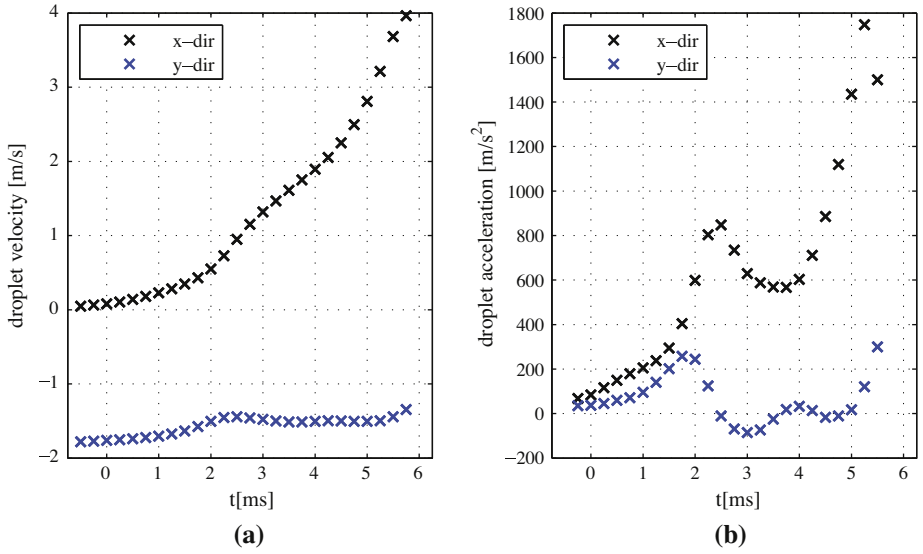

Fig. 13. Horizontal and vertical (a) velocities and (b) accelerations calculated with the central difference method for the conditions leading to the sheet-thinning morphology.

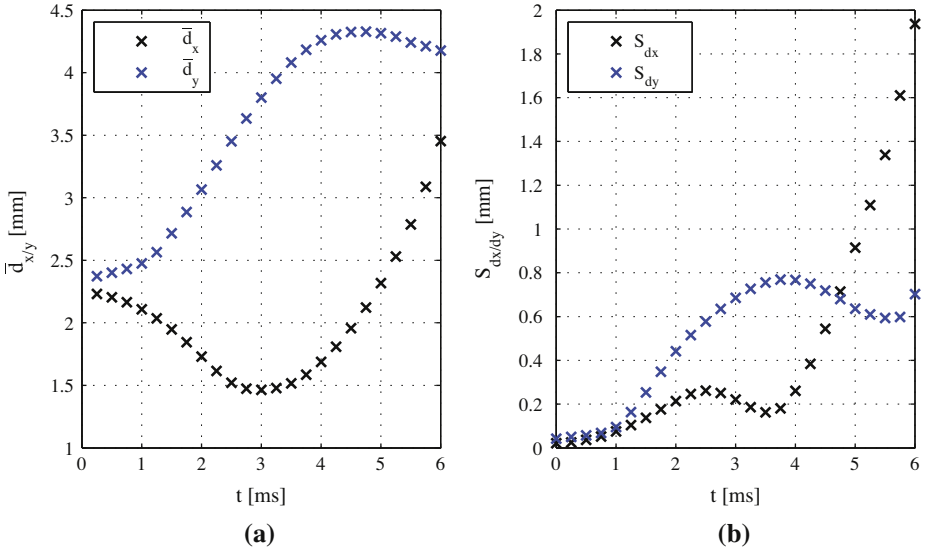

Fig. 14. (a) Mean droplet extent in the x-direction, $\bar{d}_x$, and y-direction, $\bar{d}_y$, and (b) the associated standard deviations for the conditions leading to the sheet-thinning morphology.

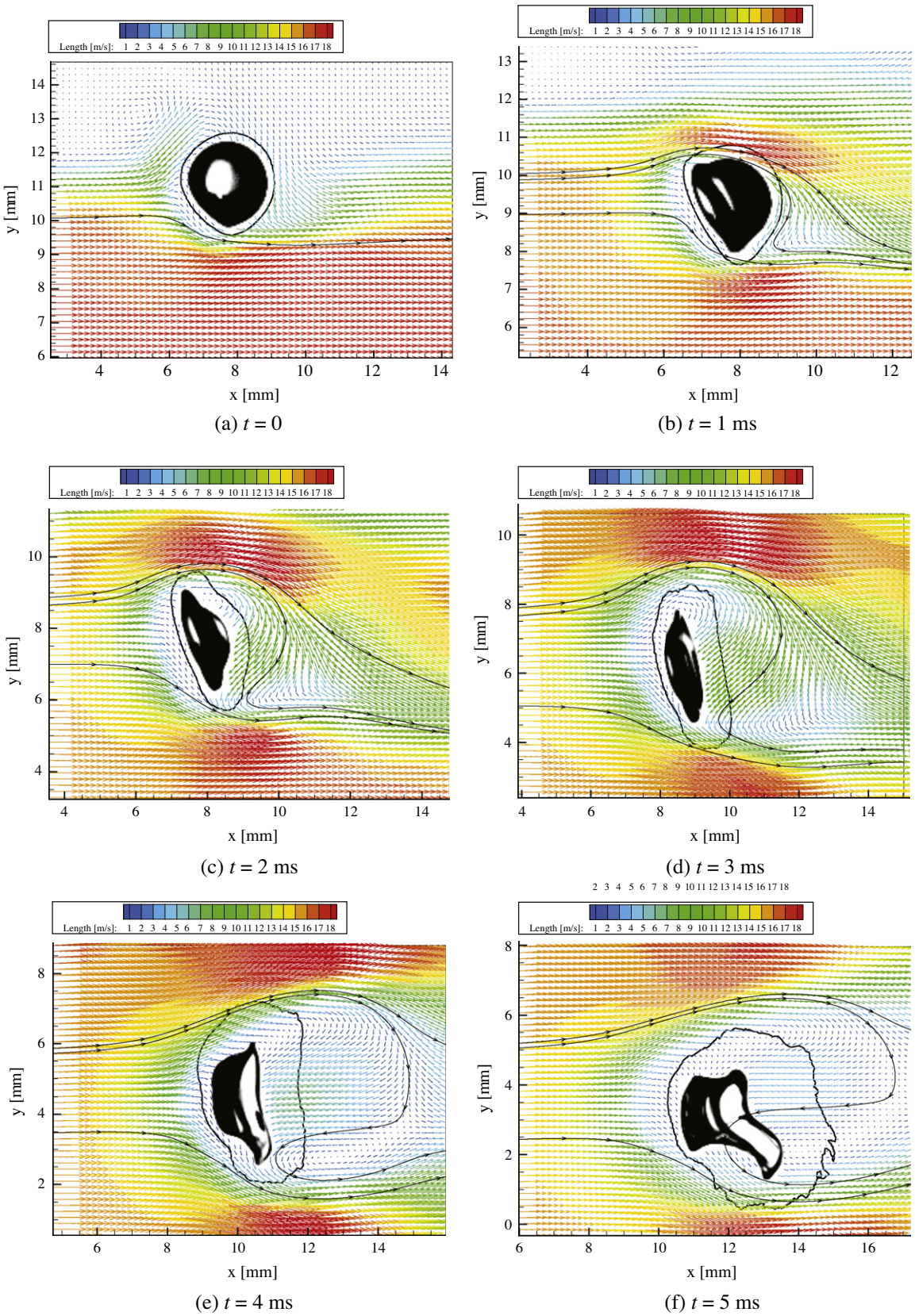

Fig. 15. Ensemble average velocity fields of 2000 PIV realizations at each instant of time for the conditions leading to the sheet-thinning morphology. Contour defines the region of 95% probability of the droplet outer-extent. A representative, instantaneous droplet shape is shown at the approximate mean droplet location. Note the shift in horizontal and vertical axes between figures. (For interpretation to colours in this figure, the reader is referred to the web version of this paper.)

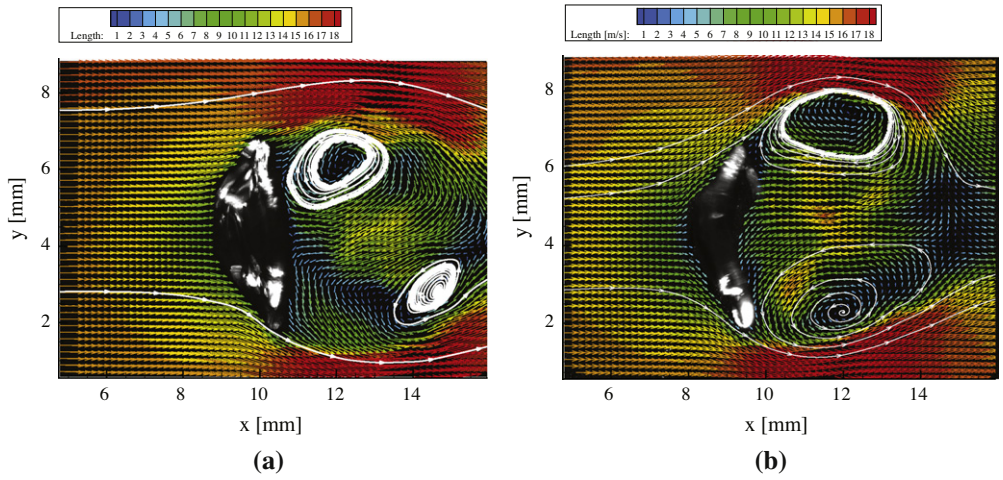

Fig. 16. Instantaneous PIV realizations at $t = 4$ ms for the conditions leading to the sheet-thinning morphology. (For interpretation to colours in this figure, the reader is referred to the web version of this paper.)

16 m/s and the mixing layer of the jet can be observed. Approximately 1 ms after that, a wake forms and is detected throughout the remaining time realizations (Fig. 15b–f). A recirculation area in the wake of the droplet, which was described for the bag breakup case, is again observed. The velocity of the backflow is about 6–7 m/s. This is higher in magnitude compared to the bag breakup case but relatively similar when considered as a percentage of free stream velocity (38–44% of the freestream velocity). Due to strong reflections from the droplet's surface it was not possible to acquire PIV images at delay times greater than 5 ms after the initial image. Thus it is unclear when or if the wake and the backflow region dissipate.

Fig. 16 shows two instantaneous PIV realizations at $t = 4$ ms. Similar to the bag case, the instantaneous results display distinct turbulent eddies in the wake region. For the subsequent discussion, it is important to note that some realizations display alternating vortices in the wake (Fig. 16a), while other realizations at the same time point show what appear to be symmetric twin vortices (Fig. 16b).

5. Discussion

Using a PIV configuration similar to the current work, Inamura et al. (2009) observed the generation of alternating vortices behind a drop which eventually deformed into the bag morphology, similar to Fig. 11. They concluded that the positive difference in static pressure between the upwind face of the deformed drop and the downstream wake results in the formation of the bag structure. Furthermore, at conditions leading to the multimode morphology, shown in the third row in Fig. 1, Inamura et al. (2009) observed the formation of symmetric twin vortices, similar to Fig. 16b observed here for the sheet-thinning case. They concluded that the strong backflow between the twin vortices results in a relatively high stagnation pressure on the center of downwind face of the deformed drop. Consequently, the center region is theorized to deform more slowly than the rest of the drop, resulting in the formation of the stamen within the bag as shown in the third column in the third row of Fig. 1.

For the conditions considered by Inamura et al. (2009), Re_g was approximately 2000–3500. In this investigation, Re_g is of the same order of magnitude (see Table 1). Due to the comparable Re_g, the instantaneous turbulent wake structures observed here (Figs. 11 and 16) appear qualitatively similar to that observed by Inamura et al. (2009). In particular, both investigations reveal large scale turbulent eddies. However, in this investigation the structure and location of the turbulent eddies does not appear to correlate with the breakup morphology. For example, as mentioned in the discussion of Fig. 16, for the sheet-thinning case some instantaneous realizations of the wake display flow morphologies resembling alternating vortices, while other realizations resemble symmetric twin vortices. Furthermore, the mean air flow-fields appear to contain no significant morphological differences between the bag case (Fig. 10) and the sheet-thinning case (Fig. 15). These observations seem to indicate that the gas-phase wake structure is unlikely to be the dominant physical mechanism which determines the liquid-phase fragmentation morphology. This conclusion agrees with experimental observations that the morphological transition in Fig. 1 is a strong function of *We* and has very little dependence on Re_g (Lee and Reitz, 2000). Nevertheless, to overcome the uncertainties introduced by ensemble averaging, further investigation utilizing high-speed PIV to record the temporal wake development behind single deforming drops is needed. Such investigations will allow for the elucidation of the role of the wake structure on the fragmentation process.

6. Conclusion

An experimental investigation of the mean behavior of deforming ethyl alcohol drops injected into a continuous air-jet is presented. Conditions leading to bag type and sheet-thinning type breakup are considered. The results presented include the mean drop diameter, trajectory, velocity, and extent, as well as the ensemble averaged air flow-field at select time realizations. Specific conclusions include:

(1) The experimental configuration and data processing techniques developed here are useful for the elucidation of mean flow behavior and provide an estimation of statistical deviations.
(2) Experimental results are useful for the development of physical models and validation of Eulerian–Lagrangian simulation techniques.
(3) The experimental evidence presented here indicates that the structure of the gas-phase wake may not significantly affect the transition between liquid-phase breakup morphologies.

Acknowledgments

Andreas K. Flock gratefully acknowledges the support of the Dr.-Ing. Willy Höfler Foundation during his research exchange at Purdue University. Further thanks is given to Sebastian Gepperth, Dr. Rainer Koch, and Prof. Dr. Sigmar Wittig for their support of his Diploma work at the Karlsruhe Institute of Technology.

Daniel R. Guildenbecher gratefully acknowledges the S.E.W. Eurodrive Foundation for support of his appointment as a Guest Professor at the Karlsruhe Institute of Technology. Additional thanks is given to Prof. Dr. Sigmar Wittig and Prof. Dr. E. Dan Hirleman for facilitating the research exchange.

References

American Society of Mechanical Engineers (ASME), 2005. Test Uncertainty, ASME PTC 19.1.

Apte, S.V., Gorokhovski, M., Moin, P., 2003. LES of atomizing spray with stochastic modeling of secondary breakup. Int. J. Multiphase Flow 29, 1503–1522.

Apte, S.V., Mahesh, K., Moin, P., 2009. Large-eddy simulation of evaporating spray in a coaxial combustor. P. Combust. Inst. 32, 2247–2256.

Chou, W.H., Faeth, G.M., 1998. Temporal properties of secondary drop breakup in the bag breakup regime. Int. J. Multiphase Flow 24, 889–912.

Chou, W.H., Hsiang, L.P., Faeth, G.M., 1997. Temporal properties of drop breakup in the shear breakup regime. Int. J. Multiphase Flow 23, 651–669.

Clift, R., Grace, J.R., Weber, M.E., 1978. Bubbles, Drops, and Particles. Academic Press, New York.

Dai, Z., Faeth, G.M., 2001. Temporal properties of secondary drop breakup in the multimode breakup regime. Int. J. Multiphase Flow 27, 217–236.

Driscoll, K.D., Sick, V., Gray, C., 2003. Simultaneous air/fuel-phase PIV measurements in a dense fuel spray. Exp. Fluids 35, 112–115.

Flock, A., 2011. Wake Dynamics During Aerodynamic Fragmentation of Liquid Drops. Diplomarbeit, Karlsruhe Institute of Technology, Karlsruhe, Germany.

Fox, R.W., McDonald, A.T., 1998. Introduction to Fluid Mechanics, fifth ed. Wiley, New York.

Gelfand, B.E., 1996. Droplet breakup phenomena in flows with velocity lag. Prog. Energy Combust. Sci. 22, 201–265.

Guildenbecher, D., López-Rivera, C., Sojka, P., 2009. Secondary atomization. Exp. Fluids 46, 371–402.

Guildenbecher, D.R., 2009. Secondary Atomization of Electrostatically Charged Drops. Ph.D. thesis, Purdue University, West Lafayette, Indiana, USA.

Guildenbecher, D.R., Sojka, P.E., 2011. Experimental investigation of aerodynamic fragmentation of liquid drops modified by electrostatic surface charge. Atomization Sprays 21, 139–147.

Hsiang, L.P., Faeth, G.M., 1992. Near-limit drop deformation and secondary breakup. Int. J. Multiphase Flow 18, 635–652.

Hwang, S.S., Liu, Z., Reitz, R.D., 1996. Breakup mechanisms and drag coefficients of high-speed vaporizing liquid drops. Atomization Sprays 6, 353–376.

Ibrahim, E.A., Yangt, H.Q., Przekwas, A.J., 1993. Modeling of spray droplets deformation and breakup. J. Propul. 9, 651–654.

Inamura, T., Yanaoka, H., Kawada, T., 2009. Visualization of airflow around a single droplet deformed in an airstream. Atomization Sprays 19, 667–677.

Lee, C.H., Reitz, R.D., 2000. An experimental study of the effect of gas density on the distortion and breakup mechanism of drops in high speed gas stream. Int. J. Multiphase Flow 26, 229–244.

Lefebvre, A.H., 1989. Atomization Sprays. Hemisphere Pub. Corp, New York.

Liu, A.B., Reitz, R.D., 1993. Mechanisms of air-assisted liquid atomization. Atomization Sprays 3, 55–75.

Müller, A., Koch, R., Bauer, H.J., Hehle, M., Schäfer, O., 2006. Performance of Prefilming Airblast Atomizers in Unsteady Flow Conditions. ASME Turbo Expo, Barcelona, Spain.

Nasar, G., Yule, A.J., Bending, L., 2002. Industrial Sprays and Atomization: Design, Analysis and Applications. Springer-Verlag, London.

O'Rourke, P.J., Amsden, A.A., 1987. The TAB method for numerical calculation of spray droplet breakup. In: International Fuels and Lubricants Meeting and Exposition. SAE Technical Paper Services, Toronto, Ontario.

Park, S.W., Kim, S., Lee, C.S., 2006. Breakup and atomization characteristics of monodispersed diesel droplets in a cross-flow air stream. Int. J. Multiphase Flow 32, 807–822.

Pilch, M., Erdman, C.A., 1987. Use of breakup time data and velocity history data to predict the maximum size of stable fragments for acceleration-induced breakup of a liquid drop. Int. J. Multiphase Flow 13, 741–757.

Raffel, M., Willert, C.E., Wereley, S.T., Kompenhans, J., 2007. Particle Image Velocimetry: A Practical Guide, second ed. Springer, Berlin.

Reitz, R.D., 1987. Modeling atomization processes in high-pressure vaporizing sprays. Atomisation Spray Technol. 3, 307–337.

Riddick, J.A., Bunger, W.B., 1970. Organic Solvents, Physical Properties and Methods of Purification, third ed. Wiley-Interscience, New York.

Schmehl, R., 2002. Advanced Modeling of Droplet Deformation and Breakup for CFD Analysis of Mixture Preparation. ILASS-Europe, Zaragoza.

Tanner, F.X., 1997. Liquid jet atomization and droplet breakup modeling of non-evaporating diesel fuel sprays. In: SAE International Congress and Exposition, Detroit, Michigan.

Theofanous, T.G., 2011. Aerobreakup of newtonian and viscoelastic liquids. Annu. Rev. Fluid Mech. 43, 661–690.

Trinh, H.P., Chen, C.P., Balasubramanyam, M.S., 2007. Numerical simulation of liquid jet atomization including turbulence effects. J. Eng. Gas. Turbines Power-Trans. ASME 129, 920–928.

Villermaux, E., Bossa, B., 2009. Single-drop fragmentation determines size distribution of raindrops. Nat. Phys. 5, 697–702.

Zhao, H., Liu, H.-F., Cao, X.-K., Li, W.-F., Xu, J.-L., 2011. Breakup characteristics of liquid drops in bag regime by a continuous and uniform air jet flow. Int. J. Multiphase Flow 37, 530–534.

Zhao, H., Liu, H.-F., Li, W.-F., Xu, J.-L., 2010. Morphological classification of low viscosity drop bag breakup in a continuous air jet stream. Phys. Fluids 22, 114103.